

Direct Imaging of Submicron Scale Defect-induced Birefringence in SrTiO₃ Bicrystals

E. B. McDaniel^(a) and J. W. P. Hsu^(b)

Department of Physics, University of Virginia, McCormick Road, Charlottesville, Virginia 22901

(October 18, 2018)

Abstract

Using a near-field scanning optical microscope capable of quantitative polarimetry, we map the anisotropic strain fields associated with individual submicron defects near the fusion boundaries of SrTiO₃ bicrystals. Many defects exhibit unexpected spiral-shape strain patterns, whose handedness is believed to be linked to the bicrystal synthesis process. Direct observation of these defect-induced strain fields helps explain previously observed non-uniformity in the characteristics of high temperature superconductor grain boundary junctions fabricated on SrTiO₃ bicrystals.

PACS numbers: 61.72.Hh, 07.79.Fc, 78.20.Fm, 61.72.Mn

A large amount of both experimental and theoretical work has been carried out in the attempt to achieve a thorough understanding of various mechanisms governing heteroepitaxial thin film growth. Of particular interest are inhomogeneous film growth systems, where the substrate itself is engineered to promote a desired lateral spatial pattern or feature [1] in the film growth. The general understanding of inhomogeneous growth currently lags well behind knowledge of simpler homogeneous systems. One crucial complicating factor that enters into inhomogeneous film growth is the effect of substrate-induced strain on the various physical properties of the films.

An important example of heteroepitaxial growth on engineered substrates is the growth of $\text{YBa}_2\text{Cu}_3\text{O}_7$ (YBCO) films on strontium titanate (SrTiO_3) bicrystals for the purpose of producing well-defined high-temperature superconducting (HTS) grain boundary Josephson junctions. [2] Bicrystals are made by fusing two pieces of single crystal together with a relative misalignment of their in-plane crystallographic axes. The locations of the HTS Josephson junctions are then defined by the fusion boundary of the underlying SrTiO_3 bicrystal substrates. In addition to the obvious technological applications, experimental results obtained on tricrystals made in a similar way have helped establish the fundamental symmetry of superconducting order parameters in this class of materials. [3] Despite the wide use of bicrystals and tricrystals, some problems remain unresolved. For example, Josephson junctions fabricated on the same substrates often exhibit drastically different transport characteristics, and grain boundary inhomogeneities might disturb the overlap of superconducting wavefunctions. [4] Therefore, a careful examination of how the substrate influences the YBCO film properties near the grain boundary, and hence device performance, is warranted.

Currently, most of the studies on this system have been either on transport property averaged over the entire junctions [2,5] or on microstructural characterization by transmission electron microscopy (TEM). [2,6,7] Spatial variations of transport characteristics and the relationship between structure and properties are obtained mostly through indirect inference or modeling. [8] Only recently have direct measurements of spatial inhomogeneities

of these HTS grain boundary Josephson junctions been examined. [9] In our previous work, [10] we showed that the presence of submicron size defects near the SrTiO₃ bicrystal fusion boundary can cause severe boundary wandering in the epitaxial YBCO film and has a detrimental effect on the superconducting characteristics of the HTS Josephson junctions. Due to the lack of surface topographic changes, we proposed that these defects cause strain in the surrounding substrate materials which in turn affect the YBCO thin film growth and physical properties. This study will focus on direct mapping of the strain fields associated with defects in SrTiO₃ bicrystals, which can then be used to predict *a priori* where YBCO film growth will be of poor quality. Because these defects are typically of submicron dimensions, polarimetry measurements by conventional optical techniques are inadequate. In this paper, we show how the sub-diffraction resolution of a near-field scanning optical microscope (NSOM) can be used with dynamic polarization-modulation (PM) techniques to achieve accurate, quantitative optical strain mapping with ~ 100 nm spatial resolution non-destructively and quickly.

The bicrystals [11] consist of two pieces of (001) single crystal SrTiO₃, a cubic perovskite, fused together with a relative misalignment of the in-plane crystallographic axes. The misalignments of all the bicrystals are symmetric, i.e., the [010] crystal direction is offset from the boundary direction by 12° (18°) on one side of the bicrystal and -12° (-18°) on the other side for 24° (36°) bicrystals. [12] The bicrystals are 1 cm x 1 cm x 0.5 mm and have been polished flat. Transmission NSOM images of SrTiO₃ bicrystals reveal that the optical transmission along the fusion boundary is highly non-uniform (Fig. 1(a)), containing circular dark features of 0.1 to 1 μ m in diameter. Notice that there are no topographic changes associated with most defects (Fig. 1(b)). The optical contrasts [13] of these features vary from 4% to 67%. The NSOM resolution is required to observe these defects because when we imaged the same region of the sample with the tip pulled back from the surface by approximately one wavelength of the light (λ), the defects could not be resolved in this far-field image. [14] Therefore, the defects seen in NSOM images must be located within λ of the surface (i.e., in the near-field zone) and will thus have a large effect on epitaxial film growth.

These microstructural defects are probably due to sub-surface voids that have been reported in TEM studies of similar bicrystals. [7] At the voids the local refractive index is effectively reduced from the bulk crystal and less light is collected due to refraction. [15] Consequently, the defects appear to be dark. [16]

It is well known that if a solid contains regions of materials with different elastic moduli, strain fields are found in the regions of matrix material surrounding the inhomogeneities and a uniformly applied stress will be disturbed near the inhomogeneities. [17] While the solution for ellipsoidal inhomogeneities in isotropic media is well known, [18] explicit calculations of strains in real crystalline solids can only be done by numerical methods [19] because the elastic constants depend on crystallographic directions. In the case of voids at the grain boundary of SrTiO₃ bicrystals, the calculation is further complicated because elastic constants change abruptly at the grain boundary, in addition to the being different for the inhomogeneities and the matrix. Furthermore, one need to consider the interactions between nearby inhomogeneities. Currently, there are no published theoretical calculations for strain fields associated with defects at internal grain boundaries, such as the case we report here. Thus, direct experimental measurements are needed to advance the current knowledge in this field.

As a cubic perovskite crystal ($m3m$), SrTiO₃ is optically isotropic with negligible absorption in the visible range. Presence of strain fields will, however, change the refractive index. Thus, a non-zero birefringence, the difference in refractive index (Δn) experienced by the two eigen-polarizations, is a quantitative measure of local anisotropic strain fields. The NSOM experiments were done in air at room temperature with an instrument capable of operation both in transmission mode [20] and in linear birefringence imaging mode. [21] Dynamic birefringence measurements are performed by incorporating a photoelastic modulator (PEM) in the optical path to vary the polarization state of the light at 50 kHz. [22] Detailed description on the design and performance of the polarization modulation NSOM has been reported in a separate publication. [23] The physical quantity measured in this experiment is the linear retardance, which is the phase difference acquired by the two orthogonal,

linear eigen-polarizations media after raveling through an anisotropic media. Retardance and birefringence are linearly related. The linear retardance (birefringence) information is contained in the signal components at the fundamental PEM modulation frequency ($1f$) and at the second harmonic ($2f$), while the DC component is directly proportional to the transmittance of the sample and the laser intensity. The dependence of the $1f$ and $2f$ components on sample transmittance and overall intensity fluctuations can therefore be removed by dividing out the DC signal. To obtain both the magnitude and the orientation of the local sample linear retardance, the demodulated $1f/DC$ and $2f/DC$ signals are recorded simultaneously at the same sample position. As the sample is moved relative to the tip, images based on each of these signals are constructed. The linear retardance magnitude (ϕ) and relative optic axis orientation (θ) of the sample at a given point can be calculated from the simultaneously recorded $1f/DC$ and $2f/DC$ data according to [23]

$$\phi = \sin^{-1} \sqrt{\frac{(1f/DC)^2}{(2J_1(\delta_0))^2} + \frac{(2f/DC)^2}{(2J_2(\delta_0))^2}}$$

and

$$\theta = \tan^{-1} \left[\frac{(2f/DC)J_1(\delta_0)}{-(1f/DC)J_2(\delta_0)} \right],$$

where J_1 and J_2 are the first and second order Bessel functions, δ_0 is the amplitude of the PEM modulation, ϕ is the magnitude of the retardance of the sample, and θ is the relative orientation of the local optical axis of the sample. A PEM modulation amplitude δ_0 of 2.405 radians (the first zero of J_0) was chosen so that the DC signal is independent of sample retardance. [24] To accurately measure linear retardance quantitatively, we developed a method to prevent the unwanted retardance due to the fiber and the tip from contaminating the sample retardance. [23] Before the sample was inserted for measurements, the linear retardance of the system is nulled to the noise limit.

The transmission NSOM image of an individual defect in a 24° bicrystal is shown in Fig. 2(a), while Fig. 2(b) shows the corresponding ϕ image. Linecuts across the two images are shown in Fig. 2(c) and 2(d), respectively. In the ϕ images, the grayscale ranges from zero (black) to 0.05 radian (white). Recall that ϕ is the magnitude of the total linear retardance

and therefore has only positive values. ϕ is related to Δn by $\Delta n = \lambda\phi/2\pi d$, where d is the distance over which the change in phase is acquired. The strain ϵ associated with Δn for a cubic material is given by $\epsilon = 2\Delta n/n^3(\Delta p)$, [25] where $n = 2.376$ for SrTiO₃ at 670 nm [26] and Δp is related to photoelastic constants for SrTiO₃. When the strain is compressive or tensile along the [100] or [010] crystallographic directions, $\Delta p = p_{11} - p_{12}$ which has the value of 0.144 for SrTiO₃. [27] For compressive or tensile strains along the [110] directions or shear strains, Δp is replaced by [25,27] $2p_{44} = 0.055$. To calculate other strains, one must separate them into these components. Since we do not induce the strain externally, we take $\Delta p \sim p_{avg} \sim 0.10$ when extracting strain values from measured birefringence values.

As discussed above, in SrTiO₃ a non-zero ϕ indicates the presence of local anisotropic strain. We found that the lateral dimensions of the retardance patterns are larger than the physical defect sizes appearing in the transmission images, as expected because strain fields propagate beyond the defects themselves. From Fig. 2(d), it is evident that at the location of the defect, ϕ does not decay monotonically away from boundary, but oscillates. The low ϕ regions between two high ϕ regions are nodal planes (lines) between a compressive and a tensile region. This non-monotonic dependence can only result from multiple sources of strain. In this case, strains from both the void and the fusion boundary contribute. When linecuts perpendicular to the boundary are taken well away from the defects, we find that ϕ does decay monotonically from a non-zero value at the fusion boundary to the background value, indicating further support that the oscillations in ϕ near the defects are the result of both voids and boundary. The unexpected symmetry-breaking spiral pattern shown in Fig. 2(b) was found to accompany many, though not all, defects on the 24° bicrystals. We discuss the possible origins later in the paper. The retardance patterns of the same defect are reproducible when imaged with different tips.

As seen in Fig. 2(c) and 2(d), maximum values of optical contrast and ϕ associated with each defect can be obtained despite the complex patterns in the ϕ images. We found that defects with greater optical contrast in the transmission NSOM images usually have greater ϕ associated with them. The plot in Fig. 3 shows maximum ϕ vs. maximum optical contrast

for 15 defects from three 24° bicrystals and 6 defects from a 36° bicrystal. Defects on the 24° bicrystal #1 (from an older batch) showed, on average, higher optical contrast and higher maximum ϕ than on the 24° bicrystals #2 and #3. Defects on the 36° bicrystal, however, showed higher optical contrast and maximum ϕ than any of the 24° bicrystals. The optical contrast ranges from 4% to 23% for defects on the 24° bicrystals, and from 24% to 67% for defects on the 36° bicrystal. The maximum ϕ for defects on the 24° bicrystals included in the plot ranges from 0.016 radians to 0.087 radians, and ranges from 0.030 radians to 0.22 radians for defects on the 36° bicrystal. The plotted points are also distinguished based on the particular objective used for light collection. Small systematic differences were noted in the maximum ϕ when the same defects were imaged using different collection optics, with slightly higher ϕ values measured with lower numerical aperture (NA) collection objectives. [28] Also of note in Fig. 3 are the two points which represent same defect on 24° bicrystal #2 imaged with different tips. The difference in these two measurements, $\leq 10\%$, is an estimate of the accuracy in our determination of ϕ .

Despite this general trend in the plot, it is not possible to predict the linear retardance based only on the *DC* optical contrast, as evidenced by the scatter. Fig. 4(a) shows two defects on the 36° bicrystal which are similar in size and optical contrast, while Fig. 4(b) shows that one has a much stronger signature in the ϕ image. The optical contrast is 40% for the lower and 33% for the upper defect. However, the maximum ϕ is 0.084 radians for the lower and almost none for the upper defect. Since the density of defects on the 36° bicrystal is substantially higher than on the 24° bicrystals, [14] the strain fields from neighboring defects overlap each other on the 36° bicrystal, as can be seen in Fig. 4(b). Since 36.8° is a special grain boundary consisting mainly of symmetric segments, [7] one might expect the 36.8° boundary to contain fewer defects. Our results show the contrary. Since the 36° bicrystal we studied is from an older batch, these defects are probably process related.

When obtaining Δn from ϕ , there is a difference between NSOM and conventional far-field measurements. Though the light travels through the entire thickness of the sample, only features within approximately λ of the surface can cause changes over the small scan size

of NSOM images. The bulk of the crystal contributes an overall background, and features beyond λ can produce slowly varying features only. [23] The retardance patterns associated with these defects, however, have features that are ~ 100 nm. Therefore, they must be due to strain fields near the surface. For these features of interest, then, we take $d \sim \lambda$. This results in a maximum Δn of .014 for the defects on the 24° bicrystals and .035 for defects on the 36° bicrystal. These birefringence values correspond to maximum strain of 0.021 for defects on the 24° bicrystals and of 0.052 for defects on the 36° bicrystal.

The spiral shape of the strain patterns is unexpected, in that it breaks the reflection symmetry of the boundary. Inclusions of different thermal contraction constants or lattice constants in a bulk cubic crystal results in two- or four-fold symmetric patterns [29] and not the symmetry-breaking strain patterns observed here. However, the defects we study in this paper are not solid inhomogeneities, but are voids that were formed at high temperatures during the fusion process. The surface tension of the surrounding SrTiO₃ surfaces plays a role in determining residual strain when the samples are cooled down. The presence of a bicrystal boundary makes the problem even more complicated because the elastic constants change abruptly at the boundary due to a change in the crystallographic direction. Furthermore, using NSOM we are probing near-surface defects. The surface may allow the strain from the defect to relax. In addition, the physical and chemical properties of the surface region might be different from the bulk. Non-cubic strontium and titanium rich phases near the surface have been observed to form at the elevated temperatures. [30] We also found that defects with clear spiral patterns in the same batch of 24° samples all show the same handedness. This implies a connection to some macroscopic phenomenon, such as a twisting motion between the two halves of bicrystals that happens after the fusion process has initiated. [31] Despite the spiral shape, the observed retardance patterns are not due to screw dislocations. Modeling the sample as a cubic crystal with no boundary, our calculations show that the spiral shape cannot be explained by the birefringence associated with the strain field from a dislocation [32] in the bulk. Furthermore, TEM results do not show screw dislocations in SrTiO₃ bicrystals of such large misalignment angles.

In summary, we report a direct and quantitative measurement of anisotropic strain fields associated with near-surface defects at the fusion boundary of SrTiO₃ bicrystals with 100 nm spatial resolution. The results reveal unexpected strain patterns that we argue are linked to problems in the fusion process. The combination of dynamic polarimetry and NSOM leads to high sensitivity and submicron resolution. This technique will be useful in studying how strain from substrates or engineered patterns influences film growth and physical properties in a broad range of heteroepitaxial growth systems.

We thank J. Z. Sun for two of the bicrystals, D. Vanderbilt, J. Mitchell, R. Shneck, M. Kawasaki, and K. Takahashi for helpful discussions. E. B. McDaniel acknowledges the support of an ONR PhD fellowship and J. W. P. Hsu of a Sloan Foundation Research Fellowship. This work is supported by NSF DMR-9357444.

REFERENCES

- (*a*) Present address: University Research Foundation, 9221 S-7 Rumsey Rd., Columbia, MD 22045
- (*b*) To whom correspondance should be addressed. E-mail: jhsu@virginia.edu
- [1] e.g., P. M. Petroff and G. Medeiros-Ribeiro, *Mater. Res. Soc. Bull.* **21**, 50 (1996)
- [2] e.g., D. Dimos, et. al., *Phys. Rev. Lett.* **61**, 219 (1988)
- [3] C. C. Tsuei, et. al., *Phys. Rev. Lett.* **73**, 593 (1994); P. Chaudhari and S. Y. Lin, *Phys. Rev. Lett.* **72**, 1084 (1994); J. H. Miller, et. al., *Phys. Rev. Lett.* **74**, 2347 (1995)
- [4] H. Hilgenkamp, J. Mannhart, and B. Mayer, *Phys. Rev. B* **53**, 14586 (1996)
- [5] D. Dimos, P. Chaudhari, and J. Mannhart, *Phys. Rev. B* **41**, 4038 (1990); R. Gross and B. Mayer, *Physica C* **180**, 235 (1991); J. A. Alarco and E. Olsson, *Phys. Rev. B* **52**, 13625 (1995); S. Schuster, et. al., *Phys. Rev. B* **48**, 16172 (1993); K. Lee, et. al., *Physica C* **257**, 99 (1996)
- [6] B. Kabius, et. al., *Physica C* **231**, 123 (1994); D. J. Miller, et. al., *Appl. Phys. Lett.* **66**, 2561 (1995)
- [7] C. Traeholt, et. al., *Physica C* **230**, 425 (1994); J. W. Seo, et. al., *Physica C* **245**, 25 (1994)
- [8] O. M. Froehlich, et. al., *Appl. Phys. Lett.* **66**, 2289 (1995); B. M. Hinaus, R. D. Redwing, and M. S. Rzechowski, *Appl. Phys. Lett.* **70**, 517 (1997); O. Neshor and E. N. Ribak, *Appl. Phys. Lett.* **71**, 1249 (1997)
- [9] G. M. Fischer, et. al., *IEEE Trans. Appl. Supercond.* **5**, 2184 (1995); J. Mannhart et. al., *Science* **245**, 839 (1989); S. Bhattacharya, et. al., *Appl. Phys. Lett.* **62**, 3510 (1993)
- [10] E. B. McDaniel, et. al., *Appl. Phys. Lett.* **70**, 1882 (1997)

- [11] Nikko Hitech Inc., San Jose, CA
- [12] The actual angle between the two sides of a 36° bicrystal is 36.8° .
- [13] Optical contrast is defined here as change in PMT current at the dark spot from the PMT current away from the bicrystal boundary divided by the PMT current away from the boundary ($\Delta I/I_{avg}$).
- [14] J. W. P. Hsu, et. al., Mater. Res. Soc. Symp. Proc. **474**, 91 (1997)
- [15] E. B. McDaniel and J. W. P. Hsu, J. Appl. Phys. **81**, 2488 (1997)
- [16] In addition to 670 nm, we performed the transmission NSOM measurements using laser light at 568 nm, 514.5 nm, and 488 nm. The contrast increases with reducing wavelength, in agreement with the wavelength dependence of SrTiO₃ refractive index. The dependence of transmission contrast using different objectives also confirm that the observed contrast is a index not an absorption phenomenon.
- [17] G. N. Savin, *Stress Concentration around Holes*, translated by E. Gros, edited by W. Johnson, (Pergamon Press, New York, 1961), Chap. II
- [18] J. D. Eshelby, Proc. Royal Soc. London **241**, 376 (1957)
- [19] R. Shneck, et. al., Phil. Mag. A **65**, 797 (1992)
- [20] E. B. McDaniel and J. W. P. Hsu, J. Appl. Phys. **80**, 1085 (1996)
- [21] T. C. Oakberg, *Linear Birefringence and Optical Rotation*, Hinds Instruments Application Note (1993), published by Hinds Instruments, Inc. (Hillsboro, OR)
- [22] 670 nm laser light passes first through a linear polarizer (oriented at 90°), and then through a photoelastic modulator (PEM), and finally through a quarter wave plate. The PEM introduces a sinusoidally time varying phase shift $\delta_0 \sin(2\pi ft)$ into the $+45^\circ$ polarization component, where the modulation frequency f is the resonant frequency (50 kHz) of the PEM quartz element. The emerging light has a polarization state which

is varying in ellipticity at f and has its principle axis at -90° . The quarter wave plate (oriented at 0°) transforms this elliptically polarized light into linearly polarized light with its orientation varying sinusoidally at the modulation frequency. This polarized light is then coupled into a single-mode optical fiber leading to the NSOM tip. The light emitted from the tip aperture and transmitted through the sample is collected by a conventional microscope objective lens. The collected light then passes through a circular polarization analyzer which transforms polarization state variation into intensity variation before reaching a photomultiplier tube (PMT). The PMT signal therefore contains information about the birefringence of the sample and the overall transmittance of the sample.

- [23] E. B. McDaniel, S. C. McClain, and J. W. P. Hsu, *Appl. Opt.* **101**, 84 (1998)
- [24] V. K. Gupta and J. A. Kornfield, *Rev. Sci. Instrum.* **65**, 2823 (1994)
- [25] J. F. Nye, *Physical Properties of Crystals* (Clarendon, Oxford, 1985), chapter XIII.2
- [26] F. Gervais, in *Handbook of Optical Constants of Solids II*, edited by E. D. Palik (Academic, Boston, 1991) p. 1039
- [27] J. Reintjes and M. B. Schulz, *J. Appl. Phys.* **39**, 5254 (1968)
- [28] Optical contrast is measured using a 100x 0.7 NA objective.
- [29] S. Y. Shu, Z. Z. Kuo, and D. Fong, *J. Phys. (Paris) C* **6**, 186 (1980)
- [30] K. Szot, et. al., *Appl. Phys. A.* **64**, 55 (1997)
- [31] K. Takahashi, private communications
- [32] J. Weertman and J. R. Weertman, *Elementary Dislocation Theory* (Oxford, New York, 1992), chapter 2

Figure Captions:

Fig. 1 (a) Transmission and (b) topographic images taken simultaneously on a 24° SrTiO₃ bicrystal. The grayscales represent 30% optical contrast in (a) and 30 Å height difference in (b). Most of the features in the topographic image are small debris on the surface. The topographic image shows two small pits which correspond to the dark spots in the transmission image on the upper part of the image. In general, when we observe a pit near the fusion boundary, there is always a corresponding dark spot in the transmission image. However, the reverse is not the case; we observe far more dark spots in the NSOM transmission images than pits on the topographic images.

Fig. 2 $3\ \mu\text{m} \times 3\ \mu\text{m}$ (a) Transmission and (a) magnitude of linear retardance (ϕ) image for an individual defect on a 24° SrTiO₃ bicrystal. The grayscales represent 10% contrast in (a) and 0.05 radians in (b). The linecuts perpendicular to the fusion boundary indicated on (a) and (b) are shown in (c) and (d) respectively.

Fig. 3 Maximum ϕ for an individual defect vs. maximum optical contrast for 21 defects on 4 SrTiO₃ bicrystals. Different symbols are used based on the bicrystal on which they are found and the objective used for light collection. A separate symbol is also used to denote two points which represent the same defect, but imaged with two different NSOM tips.

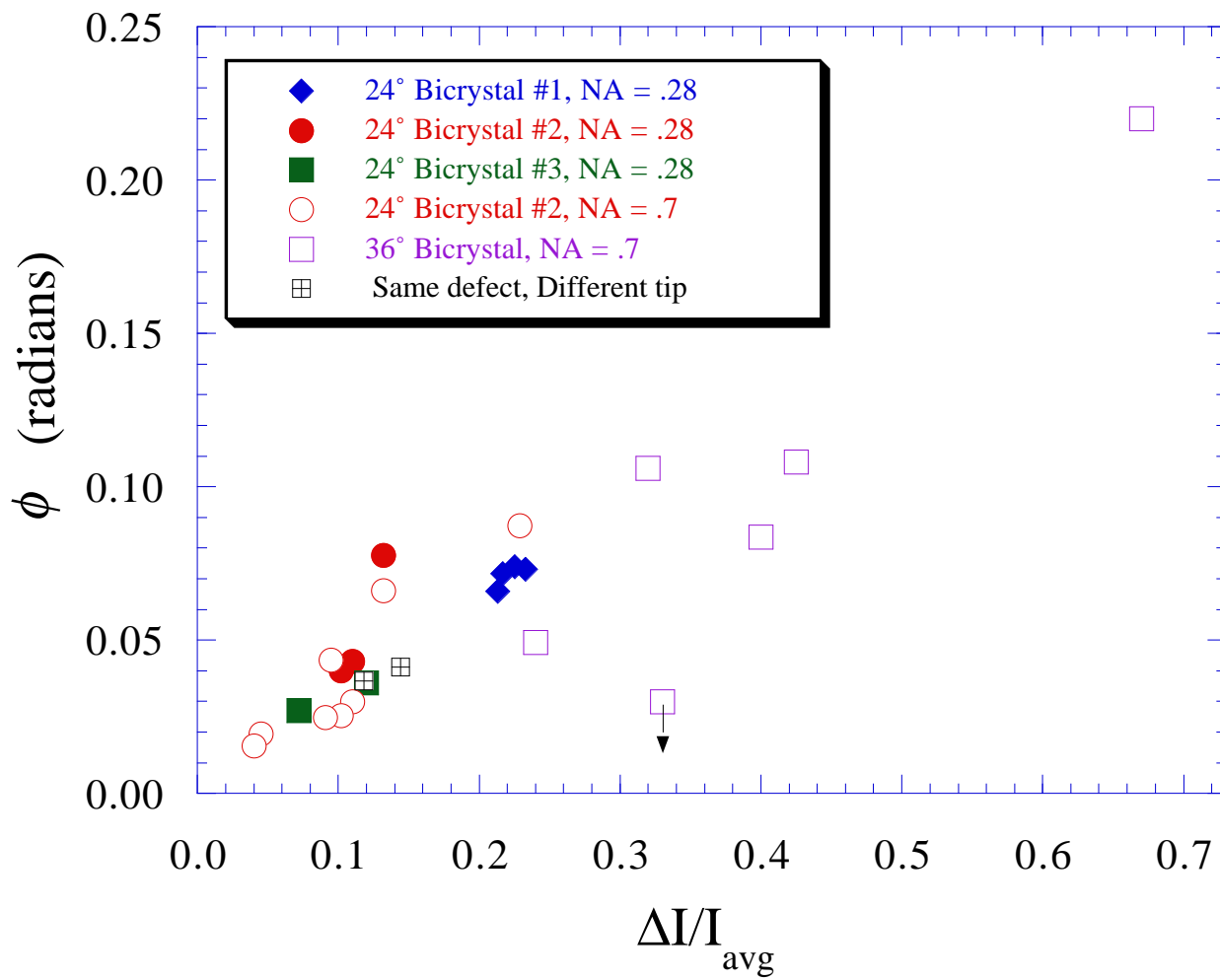
Fig. 4 (a) Transmission and (b) ϕ image of the same area on the 36° bicrystal. Two defects, marked with arrows, which look similar in the transmission image and have similar optical contrast but have very different retardance patterns and maximum ϕ values. The lower defect has 40% optical contrast and $\phi = 0.084$ radians, while the upper defect has 33% optical contrast and is not distinguishable in the ϕ image.

This figure "Fig1.jpg" is available in "jpg" format from:

<http://arxiv.org/ps/cond-mat/9802058v1>

This figure "Fig2.jpg" is available in "jpg" format from:

<http://arxiv.org/ps/cond-mat/9802058v1>



McDaniel & Hsu, Fig. 3

This figure "Fig4.jpg" is available in "jpg" format from:

<http://arxiv.org/ps/cond-mat/9802058v1>